New Elastica Geodesic Approach with Convexity Shape Prior for Region-based Active Contours and Image Segmentation

Da Chen, Laurent Cohen, Jean-Marie Mirebeau, Xue-Cheng Tai

An Elastica Geodesic Approach with Convexity Shape Prior

Da Chen
Shandong Artificial Intelligence Institute,
Qilu University of Technology
(Shandong Academy of Sciences), China
dachen.cn@hotmail.com

Laurent D. Cohen
University Paris Dauphine, PSL Research University,
CNRS, UMR 7534, CEREMADE, Paris, France.
cohen@ceremade.dauphine.fr

Jean-Marie Mirebeau
Laboratoire de mathématiques d'Orsay, CNRS,
Université Paris-Sud, Université Paris-Saclay,
91405 ORSAY, France
jean-marie.mirebeau@math.u-psud.fr

Xue-Cheng Tai
Department of Mathematics,
Hong Kong Baptist University, Hong Kong
xuechengtai@hkbu.edu.hk

Abstract

The minimal geodesic models based on the Eikonal equations are capable of finding suitable solutions in various image segmentation scenarios. Existing geodesic-based segmentation approaches usually exploit the image features in conjunction with geometric regularization terms (such as curve length or elastica length) for computing geodesic paths. In this paper, we consider a more complicated problem: finding simple and closed geodesic curves which are imposed a convexity shape prior. The proposed approach relies on an orientation-lifting strategy, by which a planar curve can be mapped to an high-dimensional orientation space. The convexity shape prior serves as a constraint for the construction of local metrics. The geodesic curves in the lifted space then can be efficiently computed through the fast marching method. In addition, we introduce a way to incorporate region-based homogeneity features into the proposed geodesic model so as to solve the region-based segmentation issues with shape prior constraints.

1. Introduction

Image segmentation is a fundamental and challenging problem posed in the fields of image analysis and computer vision. In the past decades, a large variety of segmentation approaches have been devoted to address the related segmentation problems. Among them, the energy minimization-based models integrating with priors on the target regions have proven to yield satisfactory solutions.

Prior-driven segmentation approaches. One widely considered geometric prior is to assume that the target boundaries appear to be short in terms of Euclidean curve length, by which the image noises can be suppressed in some extent. Such a first-order geometric prior has been commonly utilized in various energy minimization-based segmentation approaches such as active contours [9, 10, 38] and graph-based models [5,21]. Efficient higher order geometric priors may include the curvature-penalized length term [3, 26, 43] and data-driven weighted length [32, 42]. However, utilizing geometric regularity as a single prior is sometimes insufficient to find favorable segmentations, especially when dealing with images with complex intensity distribution. In contrast, the strategy of incorporating shape-driven priors into the objective energies can yield more accurate and efficient constraints for segmentation. These priors are often carried out via a statistical model about the target regions or contours [6, 8, 22, 23, 40]. The implementation of the shape-driven priors is capable of encouraging satisfactory segmentations, even in the absence of reliable image appearance features which are used to distinguish disjoint regions.

Recently, the shape constraints associated to the convexity and star convexity were regarded as flexible shape priors. Existing approaches in conjunction with these shape priors can be loosely categorized as either discrete or continuous types. In the discrete setting, the convexity prior [28], the star convexity prior [46], or geodesic star convexity [29] are characterized as a regularization term to construct the discrete energy functionals together with image data-driven terms. The energy minimization can be addressed by the graph cut algorithm [5]. In [27, 41], the convexity prior was incorporated into graph-based segmentation framework to solve multi-region segmentation tasks. The hedgehog-like shape prior [31] generalizes the geodesic star convexity constraint [27] to enlarge the applicable scope of the orig-

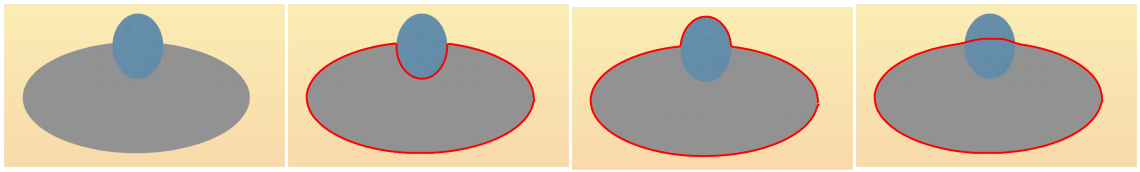

Original Image | Region-based Geodesic | Elastica Geodesic | Proposed Geodesic Model

Figure 1. Image segmentation results respectively derived from the region-based region-based geodesic model, the EM Elastica geodesic model and the proposed elastica geodesic model with convexity shape prior.

inal case. Isack *et al.* [30] proposed a flexible k-convexity shape prior model allowing overlaps between different regions. However, these graph-based approaches with convexity constraint did not consider curvature regularization.

In the continuous setting, the convexity prior is usually exploited in the active contours approaches [33, 47, 48] based on the level set formulation [39]. To be specific, in [48] the sign of the curvature was used to penalize the concave portion of the evolving contour implicitly represented by a level set function. While in [33, 47], the authors established the relationship between the Laplacian of a level set function and the convexity property of its zero-level lines, where the shape prior redefines the searching space for optimal curve. Bae *et al.* [3] illustrated that minimizing an energy regularized by a L^1-variant of Euler elastica length, which serves as a regularization term, is able to encourage the final segmentation shape to be convex. However, the convexity prior in this model is regarded as a way of implicit constraint, which heavily depends on the importance to the respective regularization term.

Geodesic models. The geodesic active contour models [7, 32, 34, 49] address the edge-based segmentation problems by minimizing a weighted curve length via a gradient descent scheme. However, the local minimization scheme may lead to demanding requirement on the initialization and high sensitivity to spurious edges or noise. Cohen and Kimmel [20] proposed a minimal path model to globally minimize a weighted curve length w.r.t. isotropic metrics [7] under the eikonal equation framework. In this paper, we are interested in finding geodesic paths with convexity shape priors. In general, the weighted length of a curve can be measured via a Finsler metric. Many geodesic approaches have contributed to develop various Finsler metrics to generate suitable geodesic paths in different situations [4, 13, 18, 19]. Chen *et al.* [12, 13] introduced to construct Randers metrics which encode region-based homogeneity features, bridging the gap between the eikonal equations and the region-based active contours. In [11, 16, 17], asymmetric metrics are exploited for image segmentation using the tool of Voronoi diagram. The curvature-penalized geodesic models [14, 25] considered an idea of orientation lifting to solve the high-order geodesic computation problems. Using suitable relaxation, the geodesic distances and geodesic paths with curvature regularization can be efficiently estimated by the Hamiltonian fast marching (HFM) method [35].

Despite great advances, only the geometric priors are utilized in existing minimal geodesic approaches. In Fig. 1, we show a comparison example for geodesic curves derived from the region-based geodesic curves [12, 13], the Euler-Mumford (EM) elastica model [14] and the proposed geodesic model with convexity shape prior. In order to bridge these gaps, we proposed a new elastica geodesic model by integrating image features and convexity shape prior, which to our best knowledge is original. In summary, the contributions of our work are threefold:

Firstly, we introduce a new elastica geodesic approach imposed with the constraint of the convexity shape prior. The convexity restriction of geodesic curves is carried out by the sign of their curvature, which is encoded into a new type of geodesic metrics established in an orientation-lifted space.

Secondly, we discuss the solutions for the computation of simple closed and convex geodesic paths. In numerical consideration, we adopt the HFM method [35] as the numerical solver, for which the stencils are adaptively generated by the proposed geodesic metric with a convexity shape constraint.

Finally, Both the region- and edge-based features are taken into account in the proposed geodesic model. The proposed model can blend the benefits from the convexity shape prior, curvature regularization and region-based homogeneity features. In addition, we propose an efficient way to incorporate user intervention for the computation of geodesic paths and for interactive image segmentation.

The structure of this paper is organized as follows. Section 2 gives the background on the elastica geodesic model and the Eikonal active contour model. The new elastica geodesic models with convexity shape prior are presented in Sections 3 and 4. The experimental results and the conclusion are respectively presented in Sections 5 and 6.

2. Background

Notations. Let $\mathbb{M} := \Omega \times \mathbb{S}^1$ be an orientation-lifted space, where $\Omega \subset \mathbb{R}^2$ is a bounded domain, and $\mathbb{S}^1 := \mathbb{R}/2\pi\mathbb{Z}$ can be identified with $[0, 2\pi[$ equipped with a periodic boundary condition. A point $\mathbf{x} = (x, \theta)$ is a pair comprised of a *physical* component x and an angular coordinate θ. For each $\mathbf{x} \in \mathbb{M}$, we denote by $\dot{\mathbf{x}} = (\dot{x}, \dot{\theta}) \in \mathbb{R}^2 \times \mathbb{R}$ a tangent vector

at $\mathbf{x}$. In the following, we use the notation $\mathbb{E} := \mathbb{R}^2 \times \mathbb{R}$ to represent the tangent space to $\mathbb{M}$ at any base point $\mathbf{x}$. In addition, we denote by $a_+ := \max\{0, a\}$ the positive part of a real number $a \in \mathbb{R}$, and let by convention $a_+^2 := (a_+)^2$.

2.1. EM Geodesic Model

Orientation lifting for curvature representation. The proposed model with convexity shape prior is established partially upon the curvature-penalized geodesic models [14, 25, 35]. The foundation of these models is to evaluate curvature using an orientation lifting. Consider a smooth curve $\gamma : [0,1] \to \Omega$, with non-vanishing velocity[1]. Then there exists a unique $\eta : [0,1] \to \mathbb{S}^1$ obeying for all $\varrho \in [0,1]$

$$\gamma'(\varrho) = (\cos\eta(\varrho), \sin\eta(\varrho))^T \, \|\gamma'(\varrho)\|. \tag{1}$$

In other words, $\eta(\varrho)$ encodes the tangent direction at $\gamma(\varrho)$. By Eq. (1), we define the orientation-lifted curve

$$\mathbf{\Gamma} = (\gamma, \eta) : \varrho \in [0,1] \mapsto \mathbf{\Gamma}(\varrho) \in \mathbb{M}, \tag{2}$$

whose first-order derivative is defined as $\mathbf{\Gamma}'(\varrho) = (\gamma'(\varrho), \eta'(\varrho)) \in \mathbb{E}$. In addition, the curvature $\kappa : [0,1] \to \mathbb{R}$ of the smooth curve γ is obtained as

$$\kappa(\varrho) = \eta'(\varrho) / \|\gamma'(\varrho)\|. \tag{3}$$

We refer to γ as the physical projection of $\mathbf{\Gamma}$.

Euler-Mumford elastica approach. In [14], the authors introduced a weighted curve length with curvature penalty, defined as follows for a smooth curve γ

$$L^{\mathrm{EM}}(\gamma) := \int_0^1 \psi(\gamma(\varrho), \eta(\varrho)) \, (1 + \beta^2 \kappa(\varrho)^2) \|\gamma'(\varrho)\| d\varrho.$$

The parameter $\beta \in \mathbb{R}^+$ has the dimension of a radius of curvature, and modulates the strength of the curvature penalty. For simplicity, and up to a rescaling argument, we assume $\beta = 1$ in the rest of this description. The cost function $\psi : \mathbb{M} \to \mathbb{R}^+$ is orientation-dependent and derived from image gradients [14]. A defect of L^{EM} is that it features second-order derivatives of γ, implicitly through the curvature κ, and is thus not directly amenable to global optimization via optimal control methods. Accordingly, an equivalent energy $\mathcal{L}^{\mathrm{EM}}$ is defined using the orientation lifting (2)

$$\mathcal{L}^{\mathrm{EM}}(\mathbf{\Gamma}) = \int_0^1 \psi(\mathbf{\Gamma}(\varrho)) \, \mathcal{F}^{\mathrm{EM}}(\mathbf{\Gamma}(\varrho), \mathbf{\Gamma}'(\varrho)) \, d\varrho, \tag{4}$$

where $\mathcal{F}^{\mathrm{EM}} : \mathbb{M} \times \mathbb{E} \to [0, \infty]$ is a Finsler metric defined for any point $\mathbf{x} = (x, \theta) \in \mathbb{M}$ and any non-zero vector $\dot{\mathbf{x}} = (\dot{x}, \dot{\theta}) \in \mathbb{E}$ as follows

$$\mathcal{F}^{\mathrm{EM}}(\mathbf{x}, \dot{\mathbf{x}}) = \begin{cases} \|\dot{x}\| + \frac{\dot{\theta}^2}{\|\dot{x}\|}, & \text{if } \dot{x} \propto \vartheta_\theta, \\ \infty, & \text{otherwise,} \end{cases} \tag{5}$$

[1]The non-vanishing velocity assumption is implicit in the sequel.

where $\vartheta_\theta = (\cos\theta, \sin\theta)^T$ is the unit vector related to $\theta \in \mathbb{S}^1$, and "$\propto$" indicates positive collinearity. The equivalence of $\mathcal{L}^{\mathrm{EM}}$ with L^{EM} follows from the expression (3) of the curvature κ. In order to compute the minimal geodesic curve from a source point $\mathbf{p} \in \mathbb{M}$ to a target point $\mathbf{x} \in \mathbb{M}$, we first estimate a geodesic distance map $\mathcal{D}_{\mathbf{p}} : \mathbb{M} \to [0, \infty)$

$$\mathcal{D}_{\mathbf{p}}(\mathbf{x}) = \inf_{\mathbf{\Gamma}} \{\mathcal{L}^{\mathrm{EM}}(\mathbf{\Gamma}); \; s.t. \; \mathbf{\Gamma}(0) = \mathbf{p}, \; \mathbf{\Gamma}(1) = \mathbf{x}\}.$$

In the following, we omit the dependence of the distance map $\mathcal{D} := \mathcal{D}_{\mathbf{p}}$ on the source point $\mathbf{p}$. This map is the viscosity solution to an eikonal equation based on the Hamiltonian $\mathcal{H}^{\mathrm{EM}}$ of the model [35, 44]

$$\mathcal{H}^{\mathrm{EM}}_{\mathbf{x}}(d\mathcal{D}(\mathbf{x})) = \tfrac{1}{2}\psi(\mathbf{x})^2, \quad \forall \mathbf{x} \in \mathbb{M} \backslash \{\mathbf{p}\}, \tag{6}$$

with $\mathcal{D}(\mathbf{p}) = 0$ and outflow boundary condition on $\partial\mathbb{M}$, where $d\mathcal{D}$ is the differential of $\mathcal{D}$. The Hamiltonian $\mathcal{H}^{\mathrm{EM}}$ is defined from the metric $\mathcal{F}^{\mathrm{EM}}$ by Legendre-Fenchel duality

$$\mathcal{H}^{\mathrm{EM}}_{\mathbf{x}}(\hat{\mathbf{x}}) = \tfrac{1}{8}\Big(\langle \hat{x}, \vartheta_\theta \rangle + \sqrt{\langle \hat{x}, \vartheta_\theta \rangle^2 + \hat{\theta}^2}\Big)^2, \tag{7}$$

for any base point $\mathbf{x} = (x, \theta) \in \mathbb{M}$ and any co-tangent vector $\hat{\mathbf{x}} = (\hat{x}, \hat{\theta}) \in \mathbb{R}^2 \times \mathbb{R}$. An equivalent integral expression of $\mathcal{H}^{\mathrm{EM}}$ can be derived

$$\mathcal{H}^{\mathrm{EM}}_{\mathbf{x}}(\hat{\mathbf{x}}) = \tfrac{3}{8} \int_{-\pi/2}^{\pi/2} \big(\langle \hat{x}, \vartheta_\theta \rangle \cos\varphi + \hat{\theta} \sin\varphi\big)_+^2 \cos\varphi d\varphi. \tag{8}$$

Using the Fejer quadrature rule for integrals, and techniques from discrete geometry, one obtains the approximation [35]

$$\mathcal{H}^{\mathrm{EM}}_{\mathbf{x}}(\hat{\mathbf{x}}) = \tfrac{1}{2} \sum_{1 \le i \le I} \rho_i^\theta \langle \hat{\mathbf{x}}, \dot{\mathbf{e}}_i^\theta \rangle_+^2 + \|\hat{\mathbf{x}}\|^2 \mathcal{O}(\varepsilon^2), \tag{9}$$

where I is a positive integer, $\rho_i^\theta \ge 0$ is a non-negative weight associated to θ, and $\dot{\mathbf{e}}_i^\theta \in \mathbb{Z}^3$ is an offset with integer components, for all $1 \le i \le I$. The construction [35] involves a relaxation parameter $\varepsilon > 0$, chosen in practice as $\varepsilon = 0.1$ with $I = 30$ offsets. A finite differences discretization of the eikonal equation (6), is obtained as a result

$$\sum_{1 \le i \le I} \rho_i^\theta \Big(\tfrac{\mathcal{D}(\mathbf{x}) - \mathcal{D}(\mathbf{x} - h\dot{\mathbf{e}}_i^\theta)}{h} \Big)_+^2 = \psi(\mathbf{x})^2, \tag{10}$$

with consistency error $\mathcal{O}(h + \varepsilon^2)$, where $h > 0$ is the grid scale. The numerical solution to (10) can be accurately estimated by the HFM method [35, 37], see Section 4.

Once the map $\mathcal{D}$ is estimated, a geodesic $\mathcal{G}$ from the source point $\mathbf{p}$ to any target $\mathbf{x} \in \mathbb{M}$, can be *backtracked*, by solving a simple ODE backwards in time. Namely one sets $\mathcal{G}(T) = \mathbf{x}$, where $T = \mathcal{D}(\mathbf{x})$ is the arrival time, and $\mathcal{G}'(\varrho) = \mathbf{V}(\mathcal{G}(\varrho))$ for all $\varrho \in [0, T]$, where the geodesic flow $\mathbf{V}$ is obtained symbolically and numerically

$$\mathbf{V}(\mathbf{x}) = \frac{d\mathcal{H}^{\mathrm{EM}}_{\mathbf{x}}}{d\hat{\mathbf{x}}}(d\mathcal{D}(\mathbf{x})), \tag{11}$$

$$= \sum_{1 \le i \le I} \rho_i^\theta \Big(\tfrac{\mathcal{D}(\mathbf{x}) - \mathcal{D}(\mathbf{x} - h\dot{\mathbf{e}}_i^\theta)}{h} \Big)_+ \dot{\mathbf{e}}_i^\theta + \mathcal{O}(h). \tag{12}$$

Then one can re-parameterize $\mathcal{G}$ to generate a new geodesic path $\mathcal{G}_{\mathbf{p},\mathbf{x}}$ defined over the range $[0,1]$.

2.2. Region-based Eikonal Active Contour Model

We briefly review the region-based Eikonal active contour (EAC) model [13, 15], which is used in this paper to build the cost function ψ in Eq. (5). We start from a typical active contour energy comprising of a region-based homogeneity term E_{r} and a regularization term E_{e}

$$E(\mathcal{C}) := \mu E_{\mathrm{r}}(\mathcal{C}) + E_{\mathrm{e}}(\mathcal{C}), \tag{13}$$

where $\mu \in \mathbb{R}^+$ is a weight parameter and $\mathcal{C} : [0,1] \to \Omega$ is a closed contour with counter-clockwise order. The component E_{e} is a weighted curve length associated to a Riemannian metric, of the form $E_{\mathrm{e}}(\mathcal{C}) = \int_0^1 \|\mathcal{C}'(\varrho)\|_{\mathcal{M}(\mathcal{C})} d\varrho$. The metric tensor $\mathcal{M}$ is here derived from the image gradients, and such that $\sqrt{\langle \dot{x}, \mathcal{M}(x)\dot{x}\rangle} = \|\dot{x}\|_{\mathcal{M}(x)}$ is low [14] if an edge passes through the point $x \in \Omega$ with tangent $\dot{x} \in \mathbb{R}^2$.

The region-based functional E_{r} measures the homogeneity of image features in each region. In this section, we take the region competition model [50] with the Gaussian mixture model (GMM) as an example to formulate the term E_{r}

$$E_{\mathrm{r}}(\mathcal{C}) = \int_{R_1} \xi_1(x)dx + \int_{R_2} \xi_2(x)dx,$$

where R_1 and R_2 are the regions inside and outside $\mathcal{C}$, respectively. The functions $\xi_i : \Omega \to \mathbb{R}$ measure the image homogeneity within each region R_i. In this paper, we compute each ξ_i using a Gaussian mixture model, for which the probability distribution function (PDF) $P_i(z;\Theta_i)$ are taken as a weighted sum of N Gaussian PDFs. In this case, one has $\xi_i(x) = -\log\big(P_i(f(x);\Theta_i)\big),\ \forall x \in \Omega$, where Θ_i are the parameters of the GMM and $f : \Omega \to \mathbb{R}^d$ is a gray level image for $d = 1$ or a color image for $d = 3$.

In the EAC model [12, 13, 15], a key ingredient is to express, using Stokes theorem, the energy (13) as a weighted curve length. In other words, $E(\mathcal{C}) \approx \mathcal{L}^{\mathrm{EAC}}(\mathcal{C}) + c$, where c is a constant and where

$$\mathcal{L}^{\mathrm{EAC}}(\mathcal{C}) = \int_0^1 \big(\|\mathcal{C}'\|_{\mathcal{M}(\mathcal{C})} + \mu\langle \omega(\mathcal{C}), \mathcal{C}'\rangle\big) d\varrho. \tag{14}$$

The vector field $\omega : U \to \mathbb{R}^2$ is defined over an open and bounded subregion $U \subset \Omega$. As in [12, 15], it is obtained as the solution of the following linear PDE problem

$$\min \ \int_U \|\omega\|^2 dx, \ s.t. \ \operatorname{curl} \omega = \xi_1 - \xi_2 \text{ on } U.$$

The weighted curve length (14) is an instance of Randers geometry, defined by the non-symmetric metric

$$\mathcal{R}(x, \dot{x}) = \|\dot{x}\|_{\mathcal{M}(x)} + \mu\langle \omega(x), \dot{x}\rangle. \tag{15}$$

As discussed in [13, 15], the positivity of $\mathcal{R}$ can be ensured by using a sufficiently small subregion U, or invoking a new vector field induced from ω. Computing minimizers of (14) can be achieved by numerically solving an eikonal equation with Randers anisotropy, leading to a robust minimization procedure for the active contour energy (13) [12, 13, 15].

3. Elastica Curves with Convexity Prior

Definition 1 *A simple closed planar curve γ, smooth and parametrized in* counter-clockwise order*, is said convex iff its curvature κ in Eq.* (3) *is* non-negative*.*

3.1. Elastica Metric with Convexity Shape Prior

We introduced in Section 2.1 the EM elastica path length L^{EM}, which we reformulated using orientation lifting (2) and a suitable metric $\mathcal{F}^{\mathrm{EM}}$ in Eq. (5). Globally optimal geodesics can be computed numerically, by solving a generalized Eikonal PDE (6), involving a suitable Hamiltonian (7), using a finite differences scheme (10).

We take here the opposite route, starting from a modified finite differences scheme - which ensures that our approach is practical - all the way back to a variant of the elastica metric embedding the constraint that curvature is non-negative, consistently with Definition 1. The modified scheme reads

$$\textstyle\sum_{1\leq i\leq I} \tilde{\rho}_i^\theta \Big(\frac{\mathcal{D}(\mathbf{x}) - \mathcal{D}(\mathbf{x} - h\dot{\mathbf{e}}_i^\theta)}{h}\Big)_+^2 = \psi(\mathbf{x})^2, \tag{16}$$

where $\tilde{\rho}_i^\theta = \rho_i^\theta$ if $\langle \dot{\mathbf{e}}_i^\theta, (0,0,1)^T\rangle \geq 0$, and $\tilde{\rho}_i^\theta = 0$ otherwise, for all $1 \leq i \leq I$. Excluding finite differences offsets $\dot{\mathbf{e}}_i^\theta$ whose third component is negative, as we do here and in contrast with the original scheme (10), ensures that the angle θ which is the third component of $\mathbf{x} = (x, \theta) \in \mathbb{M}$ is non-decreasing as the front propagates.

Let us emphasize that the modified finite differences scheme is sufficient to fully implement the numerical method, both the Eikonal solver and the backtracking ODE, by a straightforward adaptation of the geodesic flow (11) (featuring $\mathcal{H}^{\mathrm{C}}$ and $\tilde{\rho}_i^\theta$). The computations below are thus only intended to provide insight on the nature of the PDE that is solved and of the geodesic model that is globally optimized by the method. By construction, comparing with equations (9) and (10), the modified scheme corresponds to the Hamiltonian representation

$$\mathcal{H}^{\mathrm{C}}_{\mathbf{x}}(\hat{\mathbf{x}}) = \tfrac{1}{2} \textstyle\sum_{1\leq i\leq I} \tilde{\rho}_i^\theta \langle \hat{\mathbf{x}}, \dot{\mathbf{e}}_i^\theta\rangle_+^2 + \|\hat{\mathbf{x}}\|^2 \mathcal{O}(\varepsilon^2), \tag{17}$$

where $\mathbf{x} = (x, \theta) \in \mathbb{R}^2 \times \mathbb{S}^1$ and $\hat{\mathbf{x}} = (\hat{x}, \hat{\theta}) \in \mathbb{R}^2 \times \mathbb{R}$. An exact integral expression is obtained as $I \to \infty$ and $\varepsilon \to 0$

$$\mathcal{H}^{\mathrm{C}}_{\mathbf{x}}(\hat{\mathbf{x}}) := \tfrac{3}{8} \textstyle\int_0^{\frac{\pi}{2}} \big(\langle \hat{x}, \vartheta_\theta\rangle \cos\varphi + \hat{\theta} \sin\varphi\big)_+^2 \cos\varphi \, d\varphi. \tag{18}$$

Note that the proposed integral in Eq. (18) starts at 0, instead of $-\frac{\pi}{2}$ in $\mathcal{H}^{\mathrm{EM}}$. By introducing polar coordinates, one has

$$\mathcal{H}^{\mathrm{C}}_{\mathbf{x}}(\hat{\mathbf{x}}) = r^2 \hbar^{\mathrm{C}}(\phi), \ \text{ with } \ (\langle \hat{x}, \vartheta_\theta\rangle, \hat{\theta}) = r(\cos\phi, \sin\phi),$$

where $r > 0$ and $\phi \in [-\pi, \pi]$, and where $\hbar^{\mathrm{C}}$ reads as

$$\hbar^{\mathrm{C}}(\phi) := \tfrac{3}{8} \textstyle\int_0^{\pi/2} (\cos(\varphi - \phi))_+^2 \cos\varphi \, d\varphi.$$

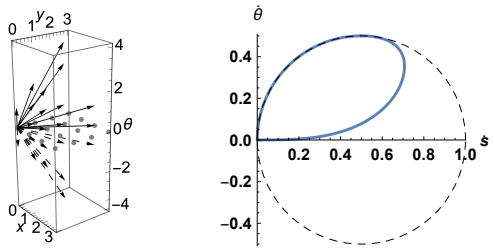

Figure 2. Left: Finite difference stencil of (10) and (16) with dashed arrows when $\langle \dot{\mathbf{e}}_i^\theta, (0,0,1)^T \rangle < 0$. Right: Unit vectors in tangent space for EM elastica model, and the variant with convexity prior. Set of all $(\dot{s}, \dot{\theta})$ such that $\mathcal{F}^{\mathrm{C}}(\mathbf{x}, (\dot{s}\vartheta_\theta, \dot{\theta})) = 1$ (solid line), and likewise for $\mathcal{F}^{\mathrm{EM}}$ (dashed line)

Distinguishing cases, we obtain a closed form expression of $\hbar^{\mathrm{C}}$, hence also of the modified Hamiltonian $\mathcal{H}^{\mathrm{C}}$, as follows

$$\hbar^{\mathrm{C}}(\phi) = \frac{1}{8}\begin{cases} 0 & \text{if } \phi \in [-\pi, -\frac{\pi}{2}], \\ 2\cos\phi + 2\cos\phi\sin\phi & \text{if } \phi \in [-\frac{\pi}{2}, 0], \\ 1 + \cos^2\phi + 2\cos\phi\sin\phi & \text{if } \phi \in [0, \frac{\pi}{2}], \\ 1 + \cos^2\phi + 2\cos\phi & \text{if } \phi \in [\frac{\pi}{2}, \pi], \end{cases}$$

The metric $\mathcal{F}^{\mathrm{C}}$ of the proposed geodesic model can be expressed in terms of the Hamiltonian $\mathcal{H}^{\mathrm{C}}$ using Legendre-Fenchel duality: $\frac{1}{2}\mathcal{F}^{\mathrm{C}}(\mathbf{x}, \dot{\mathbf{x}})^2 = \max_{\hat{\mathbf{x}}}\{\langle \hat{\mathbf{x}}, \dot{\mathbf{x}} \rangle - \mathcal{H}^{\mathrm{C}}(\mathbf{x}, \hat{\mathbf{x}})\}$. Considering a non-zero vector $\dot{\mathbf{x}} = (\dot{x}, \dot{\theta}) \in \mathbb{E}$ and denoting $\dot{s} := \|\dot{x}\|$ one has

$$\mathcal{F}^{\mathrm{C}}(\mathbf{x}, \dot{\mathbf{x}})^2 = \begin{cases} +\infty, & \text{if } \dot{\theta} < 0 \text{ or } \dot{x} \not\propto \vartheta_\theta, \\ (\dot{s} + \dot{\theta}^2/\dot{s})^2, & \text{if } 0 \le \dot{s} \le \dot{\theta}, \\ 4(\dot{s}^2 - 2\dot{s}\dot{\theta} + 2\dot{\theta}^2), & \text{if } 0 \le \dot{\theta} \le \dot{s} \le 2\dot{\theta}, \\ \frac{8}{27\dot{\theta}}(9\dot{s}\dot{\theta}^2 + \dot{s}^3 + (\dot{s}^2 - 3\dot{\theta}^2)^{\frac{3}{2}}), & \text{if } 0 \le 2\dot{\theta} \le \dot{s}. \end{cases}$$

As expected, the metric $\mathcal{F}^{\mathrm{C}}$ assigns an infinite cost to vectors whose angular velocity component $\dot{\theta}$ is negative. The path length $\mathcal{L}^{\mathrm{C}}$ associated to $\mathcal{F}^{\mathrm{C}}$, similarly to Eq. (4), is thus infinite for curves whose curvature κ takes negative values. Note that $\mathcal{F}^{\mathrm{C}}$ and $\mathcal{F}^{\mathrm{EM}}$ coincide in the regime $0 \le \dot{s} \le \dot{\theta}$ which corresponds of a curvature $\kappa = \dot{\theta}/\dot{s} \ge 1$. The set of all $(\dot{s}, \dot{\theta})$ such that $\mathcal{F}^{\mathrm{C}}(\mathbf{x}, (\dot{s}\vartheta_\theta, \dot{\theta})) = 1$, and likewise for $\mathcal{F}^{\mathrm{EM}}$, are illustrated on Fig. 2.

3.2. Searching Space for Convex Geodesics

The goal is to detect simple closed and convex curves $\mathcal{C}$ to describe target boundaries, whose orientation-lifting $\mathcal{G} = (\mathcal{C}, \eta)$ defined by (2) is a minimizer of $\mathcal{L}^{\mathrm{C}}$. For that purpose, we introduce a way of integrating the circular geodesic (CG) model [2] and the total curvature into the computation of geodesic distances associated to $\mathcal{F}^{\mathrm{C}}$. Specifically, the CG model ensures that a *closed* geodesic $\mathcal{G}$ is obtained, while the bound on the total curvature eliminates curves whose physical projection $\mathcal{C}$ has *self-intersections*.

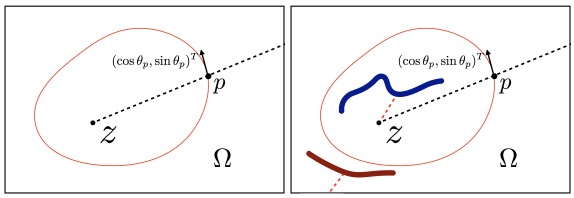

(a) (b)

Figure 3. **a** and **b**: The black dash lines and the arrows indicate the ray line $\overline{zp}$ and the direction of $(\cos\theta_p, \sin\theta_p)^T$, respectively. The red and blue curvilinear regions in figure (b) are the scribbles.

The CG Model. At the initialization stage, we exploit two points $\mathbf{p} = (p, \theta_p) \in \Omega \times \mathbb{S}^1$ and $z \in \Omega$ to set up the CG method [2], where p is placed on the boundary of the target region, with tangent orientation θ_p, and z is a point inside the target region. This initialization allows the user to guide the image segmentation in a simple and reliable manner. The ray (half line) originating from z and passing through p is denoted by $\overline{zp} \subset \Omega$. See Fig. 3a, where the angular component θ_p of $\mathbf{p}$ is indicated by the arrow $(\cos\theta_p, \sin\theta_p)^T$. We consider the following set $\Phi_1(\overline{zp})$, of curves $\gamma : [0,1] \to \Omega$ with C^2-regularity

$$\Phi_1(\overline{zp}) := \big\{\gamma;\ \mathrm{Ind}_\gamma(z) \neq 0, \gamma(0) = \gamma(1) \in \overline{zp}, \\ \gamma(\varrho) \notin \overline{zp}, \forall \varrho \in]0,1[\big\}, \quad (19)$$

where $\mathrm{Ind}_\gamma(z)$ is the winding number of γ about the point z. Any curve $\gamma \in \Phi_1(\overline{zp})$ is by construction closed and encloses the point z, as illustrated on Fig. 3a, where γ is shown as the red solid line. As in [2], the ray line $\overline{zp}$ is taken as a cut to disconnect the two sides of $\overline{zp}$ in the domain Ω, allowing to efficiently track closed geodesic paths.

Total Curvature. The total curvature $\mathrm{K}(\gamma)$ of a smooth curve $\gamma \in C^2([0,1], \Omega)$ is obtained as

$$\mathrm{K}(\gamma) = \int_0^1 \kappa(\varrho)\,\|\gamma'(\varrho)\|\,d\varrho = \int_0^1 \eta'(\varrho)\,d\varrho, \quad (20)$$

where κ is the curvature (3) and η is the orientation lifting (1). If the curvature κ is non-negative, a property ensured by our geodesic metric $\mathcal{F}^{\mathrm{C}}$ (see Section 3.1), then $\mathrm{K}(\gamma)$ coincides with the *absolute curvature* of γ. We let

$$\Phi_2 := \big\{\gamma \in C^2([0,1], \Omega);\ \mathrm{K}(\gamma) = 2\pi\big\}. \quad (21)$$

Note that $\mathrm{K}(\gamma) \in 2\pi\mathbb{Z}$ when $\gamma : [0,1] \to \Omega$ is a smooth closed curve such that $\gamma'(0) \propto \gamma'(1)$.

Search Space for Geodesic Paths. The search space for geodesic paths, for which the physical projections are simple closed and convex curves, is obtained by combining the constraints of the CG model, of prescribed total curvature, and of non-negative curvature.

Proposition 1 *Consider a smooth curve $\gamma : [0,1] \to \Omega$ with curvature $\kappa : [0,1] \to \mathbb{R}$. Then the curve γ is simple,*

Algorithm 1: Geodesic Distances Estimation

Input: A source point $\mathbf{p}$ and the set S_{end}.
Output: Geodesic distance map $\mathcal{D}$.

- Set $\mathcal{D}(\mathbf{p}) = 0$ and $\mathcal{D}(\mathbf{x}) = \infty$, $\forall x \in \mathbb{M}_h \backslash \{\mathbf{p}\}$.
- Set $\Xi(\mathbf{x}) \leftarrow$ *Trial* and $\tilde{\mathrm{K}}(\mathbf{x}) = 0$, $\forall x \in \mathbb{M}_h$.
- Construct the neighbourhood $\mathbb{N}$ and set $\mathbf{x}_{\mathrm{m}} \leftarrow \mathbf{p}$.

while $\mathbf{x}_{\mathrm{m}} \notin S_{\text{end}}$ **do**
  Find $\mathbf{x}_{\mathrm{m}}$ minimizing u among all *Trial* points.
  Set $\Xi(\mathbf{x}) \leftarrow$ *Accepted*.
  Update $\tilde{\mathrm{K}}(\mathbf{x}_{\mathrm{m}})$ using the equation (24).
  if $\tilde{\mathrm{K}}(\mathbf{x}_{\mathrm{m}}) \leq 2\pi$ **then**
    foreach $\mathbf{y} \in \tilde{\mathbb{N}}(\mathbf{x}_{\mathrm{m}})$ *s.t.* $\Xi(\mathbf{y}) =$ *Trial* **do**
      Update $\mathcal{D}(\mathbf{y})$ by solving the upwind discretization of the equation (23).
  else
    $\mathcal{D}(\mathbf{x}_{\mathrm{m}}) \leftarrow \infty$.

closed and convex, and encloses the point z, if $\gamma \in \Phi_1(\overline{zp}) \cap \Phi_2$ and $\kappa(\varrho) \geq 0$ for any $\varrho \in [0,1]$.

The search space for geodesic paths is defined as

$$\mathbf{\Phi_p} := \{\mathbf{\Gamma} = (\gamma, \eta);\ \gamma \in \Phi_1(\overline{zp}) \cap \Phi_2,\ \mathbf{\Gamma}(0) = \mathbf{\Gamma}(1) = \mathbf{p}\}.$$

Our numerical method is designed to extract the geodesic path $\mathcal{G}_{\mathbf{p}}$ which is the global optimum of the problem

$$\mathcal{G}_{\mathbf{p}} = \underset{\mathbf{\Gamma} \in \mathbf{\Phi_p}}{\arg\min} \{ \textstyle\int_0^1 \psi(\mathbf{\Gamma}(\rho))\, \mathcal{F}^{\mathrm{C}}(\mathbf{\Gamma}(\varrho), \mathbf{\Gamma}'(\varrho))\, d\varrho \}. \quad (22)$$

The orientation-lifted curves $\mathbf{\Gamma} \in \mathbf{\Phi_p}$ with finite energy obey $\mathcal{F}^{\mathrm{C}}(\mathbf{\Gamma}(\varrho), \mathbf{\Gamma}'(\varrho)) < \infty$, $\forall \varrho \in [0,1]$, which by construction of $\mathcal{F}^{\mathrm{C}}$ implies both the lifting property (1) and the non-negativity of the curvature of γ.

Remark. The proposed model allows user to provide scribbles inside and outside the target region. One can randomly choose a point x from an interior scribble, yielding a segment $[z, x]$. The segment $[z, x]$ and the scribble serve as an obstacle such that no curve is allowed to passed by it. Moreover, we can sample a point y from each individual exterior scribble, leading to a segment $[y, q]$, where $q \in \partial\Omega$ is a boundary point being such that the vector $z - y$ is proportional to $y - q$. Then, this exterior scribble and the segment $[y, q]$ form a new obstacle. We illustrate these obstacles in Fig. 3b by red dash lines.

4. Hamiltonian Fast Marching Solver

The HFM method [35–37] is a state-of-the-art numerical solver of generalized eikonal equations. It expects a domain discretized on a Cartesian grid, $\mathbb{M}_h := (\Omega \cap h\mathbb{Z}^2) \times (h\mathbb{Z} \backslash 2\pi\mathbb{Z})$ a subset of $\mathbb{M}$, where $h = 2\pi/N_\theta$ with N_θ as the number of discrete orientations.

Adaptive stencil construction. The HFM method takes its name from a specific representation or approximation of the Hamiltonian of the eikonal equation, as a sum of squares of positive parts, similar to Eq. (9) or sometimes slightly more general [37]. Crucially, this representation must only feature non-negative weights, and offsets with integer coordinates, as in Eq. (9). Its design constitutes the main originality of the HFM method, but is outside the scope of this paper. Depending on the original form of the Hamiltonian, intermediate reformulations may be employed e.g. from (7) to (8), as well as variety of tools from discrete geometry such as Voronoi's first reduction of quadratic forms [36]. This paper differs from previous works [35–37] in the sense that we start from the numerical scheme (16), and derive from it a closed form expression of the Hamiltonian $\mathcal{H}^{\mathrm{C}}$ and metric $\mathcal{F}^{\mathrm{C}}$, see Section 3.1.

The HFM method computes the numerical solution $\mathcal{D} : \mathbb{M}_h \to \mathbb{R}_0^+$ to the numerical scheme (16) (or likewise (10)). For that purpose, when adequate, the value $\mathcal{D}(\mathbf{x})$ at a point $\mathbf{x} \in \mathbb{M}_h$ is *updated* by solving locally the upwind discretization of the eikonal equation. In other words, with the notations of (16), we set $\mathcal{D}(\mathbf{x}) \leftarrow \lambda$, where λ obeys

$$\sum_{i \in \mathcal{I}(\mathbf{x})} \tilde{\rho}_i^\theta\, h^{-2} (\lambda - \mathcal{D}(\mathbf{y}_i))_+^2 = \psi(\mathbf{x})^2, \quad \text{with } \mathbf{y}_i := \mathbf{x} - h\dot{\mathbf{e}}_i^\theta, \quad (23)$$

and where $\mathcal{I}(\mathbf{x}) \subset \{1, \cdots, I\}$ is a set of valid indices. Solving for λ in Eq. (23) is a straightforward operation. Note that $\mathbf{y}_i$ is a point of the Cartesian grid $h\mathbb{Z}^3$ since the offset $\dot{\mathbf{e}}_i^\theta$ has integer coordinates, for any $1 \leq i \leq I$. However i is removed from $\mathcal{I}(\mathbf{x})$ under two conditions: (i) if $\mathbf{y}_i$ lies outside the domain $\mathbb{M}_h$, which implements outflow boundary conditions, and (ii) if the segment $[\mathbf{x}, \mathbf{y}_i]$ intersects[2] the wall $\overline{zp} \times \mathbb{S}^1$, which enforces the closedness condition (19). Notice that Point (ii) was developed specifically for the CG model.

We let $\mathbb{N}(\mathbf{x}) := \{\mathbf{y}_i;\ i \in \mathcal{I}(x)\}$ denote the stencil at $\mathbf{x}$, and $\tilde{\mathbb{N}}(\mathbf{x}) := \{\mathbf{y} \in \mathbb{M}_h;\ \mathbf{x} \in \mathbb{N}(\mathbf{y})\}$ the reversed stencil.

Single-pass HFM algorithm. At the initialization stage, the HFM method tags each grid point $\mathbf{x} \in \mathbb{M}_h$ as *Trial*. We set the geodesic distances $\mathcal{D}(\mathbf{x}) = \infty$ for all the grid points $\mathbf{x} \in \mathbb{M}_h \backslash \{\mathbf{p}\}$ and set $\mathcal{D}(\mathbf{p}) = 0$ for the source point. During the front propagation, the HFM method finds a point $\mathbf{x}_{\mathrm{m}}$ with the smallest distance value among all *Trial* points. This point $\mathbf{x}_{\mathrm{m}}$ is immediately tagged as *Accepted*. Then for each point $\mathbf{y} \in \tilde{\mathbb{N}}(\mathbf{x}_{\mathrm{m}})$ of the reversed neighborhood, the distance $\mathcal{D}(\mathbf{y})$ is updated by solving the upwind discretization of the eikonal equation (23), taking only into account the values of $\mathcal{D}$ corresponding to previously *Accepted* points.

Computation of the total curvature. In [24], the authors introduced an efficient method which can simultaneously

[2] We allow the intersection between $[\mathbf{x}, \mathbf{y}_i]$ and $\overline{zp} \times \mathbb{S}^1$ for the case $\mathbf{x} \in \overline{zp} \times \mathbb{S}^1$ and the vector $\mathbf{y}_i - \mathbf{x}$ points to the left side of $\overline{zp} \times \mathbb{S}^1$.

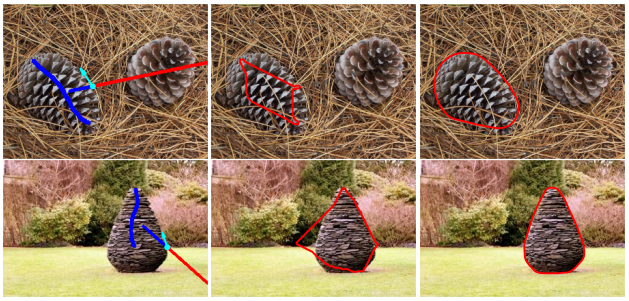

Figure 4. Qualitative comparison with the model [28]. The original images are shown in column 1. The segmentations in columns 2 and 3 are derived from [28] and the proposed model, respectively.

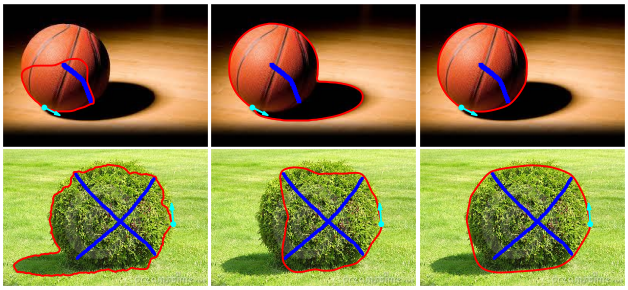

Figure 5. Qualitative comparison with the EAC model (column 1) and the original elastica model (column 2). The results in column 3 are derived from the proposed model.

compute the geodesic distances and the Euclidean distances between the source point $\mathbf{p}$ and any target point $\mathbf{x}$ in an accumulation manner. As a result, the Euclidean length of each geodesic path can be estimated without backtracking these paths, which reduces computation time. In this paper, we adapt the method of [24] to compute simultaneously the length $\mathcal{D}(\mathbf{x}) = \mathcal{L}^{\mathrm{C}}(\mathcal{G}_{\mathbf{p},\mathbf{x}})$ of the geodesic $\mathcal{G}_{\mathbf{p},\mathbf{x}} = (\gamma, \eta)$ reaching the point $\mathbf{x}$, and its total curvature $\tilde{\mathrm{K}}(\mathbf{x})$

$$\tilde{\mathrm{K}}(\mathbf{x}) := \mathrm{K}(\gamma) = \int_0^1 \eta'(\varrho) d\varrho.$$

For that purpose, we note that the total curvature map $\tilde{\mathrm{K}}$ obeys a linear PDE, involving the geodesic flow vector field $\mathbf{V} : \mathbb{M} \to \mathbb{R}^2 \times \mathbb{R}$ used in geodesic backtracking (11)

$$\langle \nabla \tilde{\mathrm{K}}, \mathbf{V} \rangle = \mathbf{V}_3, \qquad \text{where } \mathbf{V}_3 := \langle (0,0,1)^T, \mathbf{V} \rangle.$$

In addition, the numerical method yields a simple and intrinsic approximation of the geodesic flow (11), of the form $\mathbf{V}(\mathbf{x}) = \sum_{i \in \mathcal{I}(\mathbf{x})} \tau_i \dot{\mathbf{e}}_i^{\theta} + \mathcal{O}(h)$ with the notations of (23). Thus one has, using an upwind finite differences scheme

$$\Big(\sum_{i \in \mathcal{I}(x)} \tau_i \Big) \tilde{\mathrm{K}}(\mathbf{x}) = \sum_{i \in \mathcal{I}(x)} \tau_i \tilde{\mathrm{K}}(\mathbf{y}_i) + h \mathbf{V}_3(\mathbf{x}) + \mathcal{O}(h^2). \tag{24}$$

We solve for $\tilde{\mathrm{K}}(\mathbf{x})$ when the point $\mathbf{x}$ is *Accepted*, using this linear equation and omitting the $\mathcal{O}(h^2)$ term. For all $i \in \mathcal{I}(x)$ such that $\tau_i > 0$, one has $\mathcal{D}(\mathbf{x}) > \mathcal{D}(\mathbf{y}_i)$, since $\mathbf{y}_i$ was previously *Accepted*. If the value of $\tilde{\mathrm{K}}(\mathbf{x}) > 2\pi$, then we set $\mathcal{D}(\mathbf{x}) = \infty$ to avoid the self-crossing problem.

In Algorithm 1, we summarize this variant of the HFM for computing the geodesic distance map u. The front propagation is terminated when any end point $\mathbf{x}_{\mathrm{e}} \in S_{\mathrm{end}}$ is tagged as *Accepted*, where the set $S_{\mathrm{end}} \subset \mathbb{M}_h$ collects all the immediate neighbors of $\mathbf{p} = (p, \theta_p) \in \mathbb{M}_h$ on the correct side of $\overline{zp} \times \mathbb{S}^1$. The desired geodesic path, defined in Eq. (22), is then backtracked by Eq. (11).

Computation of the cost function. The length $\mathcal{L}^{\mathrm{EAC}}$ in Eq. (14) can be interpreted in the framework of Section 2.1, by choosing the cost $\psi(x,\theta) = \mathcal{R}(x, \vartheta_\theta)$, and $\beta = 0$. This leads to the possibility of integrating the regional homogeneity features and curvature regularization for tracking geodesic paths. However, such an interpretation is not what we do in this paper, opting instead for an exponential cost

$$\psi(x,\theta) = \begin{cases} \exp(\alpha \tilde{\mathcal{R}}(x, \vartheta_\theta)), & \forall x \in U, \\ \infty, & \text{otherwise} \end{cases}$$

and $\beta > 0$, where $\tilde{\mathcal{R}}(x,\theta)$ is defined as

$$\tilde{\mathcal{R}}(x,\theta) = \frac{\|\vartheta_\theta\|_{\mathcal{M}(x)}}{\max_{(\tilde{x},\tilde{\theta}) \in \mathbb{M}} \|\vartheta_{\tilde{\theta}}\|_{\mathcal{M}(\tilde{x})}} + \frac{\mu \langle \vartheta_\theta, \omega(x) \rangle}{\max_{y \in U} \|\omega(y)\|}.$$

This construction of the cost function proves to be very efficient in practice. Note that the subdomain $U \subset \Omega$ should be understood as a search space for geodesic paths such that any geodesic curve $\mathcal{G}_{\mathbf{p}} = (\mathcal{C}_{\mathbf{p}}, \eta_{\mathbf{p}})$ obeys $\mathcal{C}_{\mathbf{p}}(\varrho) \in U, \forall \varrho \in [0,1]$. Up to curve evolution scheme, the goal is to produce sequences $(\mathcal{C}_j)_{j \geq 0}$ of geodesic curves which solve the problem (22), and the subregion U at the j-th iteration is defined as a tubular neighbourhood of $\mathcal{C}_{j-1}$. The initial curve $\mathcal{C}_0$ is required to be simple, closed and convex. Since the edge-based features are independent to the evolving curves $\mathcal{C}_j$, such an initial curve $\mathcal{C}_0$ can be produced using edge-based features only, implemented by using $\psi(x,\theta) = \exp(\alpha \|\vartheta_\theta\|_{\mathcal{M}(x)} / \max_{(\tilde{x},\tilde{\theta}) \in \mathbb{M}} \|\vartheta_{\tilde{\theta}}\|_{\mathcal{M}(\tilde{x})}), \forall x \in \Omega$.

Computation time. For a given metric $\mathcal{F}^{\mathrm{C}}$ and a given grid $\mathbb{M}_h$, the computation complexity is bounded by the anisotropy ratio [35] which is determined by the relaxation parameter ε. We report the running time of Fig. 1 with $\varepsilon = 0.1$, where the size of the grid is $346 \times 599 \times 60$. The CPU-implemented HFM method requires around 38 seconds under a suitable stopping criterion, while a GPU-implemented numerical solver requires around 2.5 seconds.

5. Experimental Results

In this section, we illustrate the advantages of using the convexity shape constraint and curvature regularization for interactive image segmentation. In the following experiments, we provide scribbles within the target regions and

source positions p with tangents $(\cos\theta_p, \sin\theta_p)^T$ to set up the proposed model. Accordingly, the original point z is obtained as the barycentre point of the convex hull of the union of the scribbles and the source position.

In Fig. 4, we illustrate the qualitative comparison results with the graph-based model [28] which also features convexity shape prior. In column 1, we show the original images [1] with scribbles (blue and red curvilinear regions), and source positions with given tangents, where cyan dots represents source positions p. The cyan arrows are positively collinear to $(\cos\theta_p, \sin\theta_p)^T$. Each red line represents the small neighbourhood of the segment between the point z and the boundary $\partial\Omega$. These scribbles are taken as input for model [28]. In Fig. 4, we can see that the segmentations from the proposed model can accurately capture the desired boundaries. In contrast, the segmentation regions from [28] appear to be convex, but fail to depict the targets.

In Fig. 5, we compare the proposed model to state-of-the-art geodesic models. Specifically, the segmentation results from the EAC model [13, 15], the EM elastica model [14] and the proposed model are respectively depicted in columns 1 to 3. The cyan dots and the corresponding arrows indicate the source positions and the tangents. The blue curvilinear regions indicate the scribbles inside the target regions. For the EM elastica model, only the edge-based features are used for segmentation. From this experiment, one can point out that only the proposed model are capable of finding suitable segmentation results.

We also evaluate quantitative comparisons on 43 CT images [45], where the target regions of the test images are approximately convex. In order to illustrate the advantages of the proposed model which encodes convexity shape prior and curvature regularization, we add Gaussian noise to each test image. Two examples of these CT images are shown at the bottom of Fig. 6. The quantitative evaluation for the EAC model, the EM elastica model and the proposed model is carried out by the Jaccard Index. Here we exploit only the edge-based cost function for the EM elastica model. The boxplots of the Jaccard Index values from the considered models are exhibited at the top of Fig. 6. Again, we observe that the proposed model achieves the best performance among the compared approaches. In this experiment, we only exploit the points z and $\mathbf{p} = (p, \theta_p)$ as initialization to set up the EAC and EM elastica models. The point z for each test image is taken as the barycentre point of the target region. Each source point p is randomly chosen from the ground truth boundary, while the angular coordinate θ_p is set as the counter-clockwise tangent of the boundary at p.

6. Conclusion

In this paper, we show the possibility of integrating the convexity shape prior, the EM elastica term and the region-based homogeneity features into the computation of simple closed and convex curves. One main contribution lies at the introduction of a variant of the original EM elastica Hamiltonian in order to induce new asymmetric geodesic metrics which encode the convexity shape constraint. As a second contribution, we introduce efficient numerical solutions for computing orientation-lifted geodesic curves based on the HFM method, whose physical projection curves are simple closed and convex. Experiments show that the proposed model indeed obtains promising segmentation results.

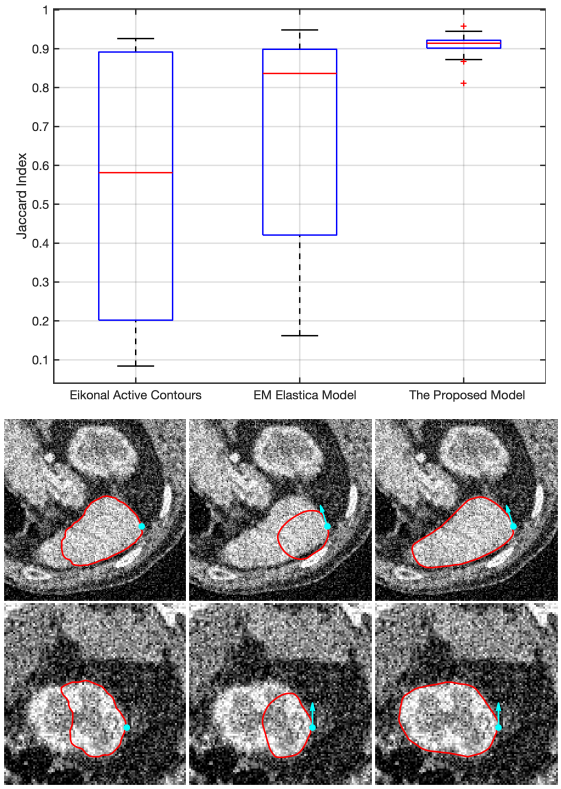

Figure 6. Top: Box plots of the Jaccard index values on 43 CT images with Gaussian noise for the EAC model, EM elastica model and the proposed model. Bottom: Segmentations on two examples of CT images, where columns 1 to 3 show the results respectively from the EAC model, EM elastica model and the proposed one.

Acknowledgement

This work was supported by the National Natural Science Foundation of China (NO. 61902224), by the French government under management of Agence Nationale de la Recherche as part of the "Investissements d'avenir" program, reference ANR-19-P3IA-0001 (PRAIRIE 3IA Institute), by new AI project towards the integration of education and industry in QLUT (NO. 2020KJC-JC01), and by the Young Taishan Scholars (NO.tsqn201909137). Tai is supported by GRF project HKBU-12300819, NSF/RGC Grant N-HKBU214-19 and RC-FNRA-IG/19-20/SCI/01.

References

[1] S. Alpert, M. Galun, A. Brandt, and R. Basri. Image segmentation by probabilistic bottom-up aggregation and cue integration. *IEEE Trans. Pattern Anal. Mach. Intell.*, 34(2):315–327, 2012. 8

[2] B. Appleton and H. Talbot. Globally optimal geodesic active contours. *J. Math. Imaging Vis.*, 23(1):67–86, 2005. 5

[3] E. Bae, X.-C. Tai, and Z. Wei. Augmented lagrangian method for an euler's elastica based segmentation model that promotes convex contours. *Inverse. Probl. Imaging*, 11(1):1–23, 2017. 1, 2

[4] F. Benmansour and L. D. Cohen. Tubular structure segmentation based on minimal path method and anisotropic enhancement. *Int. J. Comput. Vis.*, 92(2):192–210, 2011. 2

[5] Y. Boykov and G. Funka-Lea. Graph cuts and efficient N-D image segmentation. *Int. J. Comput. Vis.*, 70:109—-131, 2006. 1

[6] X. Bresson, P. Vandergheynst, and J.-P. Thiran. A variational model for object segmentation using boundary information and shape prior driven by the Mumford-Shah functional. *Int. J. Comput. Vis.*, 68(2):145–162, 2006. 1

[7] V. Caselles, R. Kimmel, and G. Sapiro. Geodesic active contours. *Int. J. Comput. Vis.*, 22(1):61–79, 1997. 2

[8] T. Chan and W. Zhu. Level set based shape prior segmentation. In *Proc. CVPR*, volume 2, pages 1164–1170. IEEE, 2005. 1

[9] T. F. Chan, S. Esedoglu, and M. Nikolova. Algorithms for finding global minimizers of image segmentation and denoising models. *SIAM J. Appl. Math.*, 66(5):1632–1648, 2006. 1

[10] T. F. Chan, B. Y. Sandberg, and L. A. Vese. Active contours without edges for vector-valued images. *J. Vis. Commun. Image Represent.*, 11(2):130–141, 2000. 1

[11] D. Chen and L. D. Cohen. Fast asymmetric fronts propagation for image segmentation. *J. Math. Imaging Vis.*, 60(6):766–783, 2018. 2

[12] D. Chen and L. D. Cohen. From active contours to minimal geodesic paths: New solutions to active contours problems by Eikonal equations. In *Handbook of Numerical Analysis*, volume 20, pages 233–271. Elsevier, 2019. 2, 4

[13] D. Chen, J.-M. Mirebeau, and L. D. Cohen. Finsler geodesics evolution model for region based active contours. In *Proc. BMVC*, 2016. 2, 4, 8

[14] D. Chen, J.-M. Mirebeau, and L. D. Cohen. Global minimum for a Finsler elastica minimal path approach. *Int. J. Comput. Vis.*, 122(3):458–483, 2017. 2, 3, 4, 8

[15] D. Chen, J.-M. Mirebeau, H. Shu, and L. D. Cohen. Eikonal region-based active contours for image segmentation. *arXiv preprint arXiv:1912.10122*, 2019. 4, 8

[16] D. Chen, J. Spencer, J. M. Mirebeau, K. Chen, and L. D. Cohen. Asymmetric geodesic distance propagation for active contours. In *Proc. BMVC*, 2018. 2

[17] D. Chen, J. Spencer, J.-M. Mirebeau, K. Chen, M. Shu, and L. D Cohen. A generalized asymmetric dual-front model for active contours and image segmentation. *IEEE Trans. Image Process.*, 30:5056–5071, 2021. 2

[18] D. Chen, J. Zhang, and L. D. Cohen. Minimal paths for tubular structure segmentation with coherence penalty and adaptive anisotropy. *IEEE Trans. Image Process.*, 28(3):1271–1284, 2019. 2

[19] D. Chen, J. Zhu, X. Zhang, M. Shu, and L. D Cohen. Geodesic paths for image segmentation with implicit region-based homogeneity enhancement. *IEEE Trans. Image Process.*, 30:5138–5153, 2021. 2

[20] L. D. Cohen and R. Kimmel. Global minimum for active contour models: A minimal path approach. *Int. J. Comput. Vis.*, 24(1):57–78, 1997. 2

[21] C. Couprie, L. Grady, L. Najman, and H. Talbot. Power watershed: A unifying graph-based optimization framework. *IEEE Trans. Pattern Anal. Mach. Intell.*, 33(7):1384–1399, 2011. 1

[22] D. Cremers, M. Rousson, and R. Deriche. A review of statistical approaches to level set segmentation: integrating color, texture, motion and shape. *Int. J. Comput. Vis.*, 72(2):195–215, 2007. 1

[23] D. Cremers, F. R. Schmidt, and F. Barthel. Shape priors in variational image segmentation: Convexity, lipschitz continuity and globally optimal solutions. In *Proc. CVPR*, pages 1–6. IEEE, 2008. 1

[24] T. Deschamps and L. D. Cohen. Fast extraction of minimal paths in 3D images and applications to virtual endoscopy. *Med. Image Anal.*, 5(4):281–299, 2001. 6, 7

[25] R. Duits, S. PL Meesters, J.-M. Mirebeau, and J. M Portegies. Optimal paths for variants of the 2D and 3D Reeds–Shepp car with applications in image analysis. *J. Math. Imag. Vis.*, 60(6):816–848, 2018. 2, 3

[26] N. Y. El-Zehiry and L. Grady. Contrast driven elastica for image segmentation. *IEEE Trans. Image Process.*, 25(6):2508–2518, 2016. 1

[27] L. Gorelick and O. Veksler. Multi-object convexity shape prior for segmentation. In *Proc. EMMCVPR*, pages 455–468. Springer, 2017. 1

[28] L. Gorelick, O. Veksler, Y. Boykov, and C. Nieuwenhuis. Convexity shape prior for binary segmentation. *IEEE Trans. Pattern Anal. Mach. Intell.*, 39(2):258–271, 2016. 1, 7, 8

[29] V. Gulshan, C. Rother, A. Criminisi, A. Blake, and A. Zisserman. Geodesic star convexity for interactive image segmentation. In *Proc. CVPR*, pages 3129–3136. IEEE, 2010. 1

[30] H. Isack, L. Gorelick, K. Ng, O. Veksler, and Y. Boykov. K-convexity shape priors for segmentation. In *Proc. ECCV*, pages 36–51, 2018. 2

[31] H. Isack, O. Veksler, M. Sonka, and Y. Boykov. Hedgehog shape priors for multi-object segmentation. In *Proc. CVPR*, pages 2434–2442, 2016. 1

[32] R. Kimmel and A. M. Bruckstein. Regularized laplacian zero crossings as optimal edge integrators. *Int. J. Comput. Vis.*, 53(3):225–243, 2003. 1, 2

[33] S. Luo, X.-C. Tai, L. Huo, Y. Wang, and R. Glowinski. Convex shape prior for multi-object segmentation using a single level set function. In *Proc. CVPR*, pages 613–621, 2019. 2

[34] J. Melonakos, E. Pichon, S. Angenent, and A. Tannenbaum. Finsler active contours. *IEEE Trans. Pattern Anal. Mach. Intell.*, 30(3):412–423, 2008. 2

[35] J.-M. Mirebeau. Fast-marching methods for curvature penalized shortest paths. *J. Math. Imag. Vis.*, 60(6):784–815, 2018. 2, 3, 6, 7

[36] J.-M. Mirebeau. Riemannian fast-marching on Cartesian grids, using Voronoi's first reduction of quadratic forms. *SIAM J. Numer. Anal.*, 57(6):2608–2655, 2019. 6

[37] J.-M. Mirebeau and J. Portegies. Hamiltonian fast marching: a numerical solver for anisotropic and non-holonomic eikonal PDEs. *Image Processing On Line*, 9:47–93, 2019. 3, 6

[38] D. Mumford and J. Shah. Optimal approximations by piecewise smooth functions and associated variational problems. *Commun. Pure Appl. Math.*, 42(5):577–685, 1989. 1

[39] S. Osher and J. A. Sethian. Fronts propagating with curvature-dependent speed: algorithms based on Hamilton-Jacobi formulations. *J. Comput. Phys.*, 79(1):12–49, 1988. 2

[40] R. Prevost, R. Cuingnet, B. Mory, L. D. Cohen, and R. Ardon. Tagged template deformation. In *Proc. MICCAI*, pages 674–681. Springer, 2014. 1

[41] L. A. Royer, D. L. Richmond, C. Rother, B. Andres, and D. Kainmueller. Convexity shape constraints for image segmentation. In *Proc. CVPR*, pages 402–410, 2016. 1

[42] C. Sagiv, N. A. Sochen, and Y. Y. Zeevi. Integrated active contours for texture segmentation. *IEEE Trans. Image Process.*, 15(6):1633–1646, 2006. 1

[43] T. Schoenemann, F. Kahl, S. Masnou, and D. Cremers. A linear framework for region-based image segmentation and inpainting involving curvature penalization. *Int. J. Comput. Vis.*, 99(1):53–68, 2012. 1

[44] J. A. Sethian and A. Vladimirsky. Ordered upwind methods for static Hamilton–Jacobi equations: Theory and algorithms. *SIAM J. Numer. Anal.*, 41(1):325–363, 2003. 3

[45] J. Spencer, K. Chen, and J. Duan. Parameter-free selective segmentation with convex variational methods. *IEEE Trans. Image Process.*, 28(5):2163–2172, 2019. 8

[46] O. Veksler. Star shape prior for graph-cut image segmentation. In *Proc. ECCV*, pages 454–467. Springer, 2008. 1

[47] S. Yan, X.-C. Tai, J. Liu, and H.-Y. Huang. Convexity shape prior for level set-based image segmentation method. *IEEE Trans. Image Process.*, 29:7141–7152, 2020. 2

[48] C. Yang, X. Shi, D. Yao, and C. Li. A level set method for convexity preserving segmentation of cardiac left ventricle. In *Proc. ICIP*, pages 2159–2163. IEEE, 2017. 2

[49] A. Yezzi, S. Kichenassamy, A. Kumar, P. Olver, and A. Tannenbaum. A geometric snake model for segmentation of medical imagery. *IEEE Trans. Med. Imaging*, 16(2):199–209, 1997. 2

[50] S. Zhu and A. Yuille. Region competition: Unifying snakes, region growing, and Bayes/MDL for multiband image segmentation. *IEEE Trans. Pattern Anal. Mach. Intell.*, 18(9):884–900, 1996. 4